A Monte Carlo feasibility study on quantitative laser-driven proton radiography

Matthias Würl[1,*], **Chiara Gianoli**[1], **Franz Siegfried Englbrecht**[1], **Jörg Schreiber**[1,2], **Katia Parodi**[1]

[1] Department of Medical Physics, Faculty of Physics, Ludwig-Maximilians-Universität München, Germany
[2] Max-Planck-Institut für Quantenoptik, Garching, Germany

Received 12 September 2019; accepted 11 May 2020

Abstract

Laser-accelerated proton bunches with kinetic energies up to several tens of MeV and at repetition rates in the order of Hz are nowadays achievable at several research centres housing high-power laser system. The unique features of such ultra-short bunches are also arousing interest in the field of radiological and biomedical applications. For many of these applications, accurate positioning of the biological target is crucial, raising the need for on-site imaging. One convenient option is proton radiography, which can exploit the polyenergetic spectrum of laser-accelerated proton bunches. We present a Monte Carlo (MC) feasibility study to assess the applicability and potential of laser-driven proton radiography of millimetre to centimetre sized objects. Our radiography setup consists of a thin time-of-flight spectrometer operated in transmission prior to the object and a pixelated silicon detector for imaging. Proton bunches with kinetic energies up to 20 MeV and up to 100 MeV were investigated. The water equivalent thickness (WET) of the traversed material is calculated from the energy deposition inside an imaging detector, using an online generated calibration curve that is based on a MC generated look-up table and the reconstructed proton energy distribution. With a dose of 43 mGy for a 1 mm thin object imaged with protons up to 20 MeV, the reconstructed WET of defined regions-of-interest was within 1.5% of the ground truth values. The spatial resolution, which strongly depends on the gap between object and imaging detector, was 2.5 lp mm^{-1} for a realistic distance of 5 mm. Due to this relatively high imaging dose, our proposed setup for laser-driven proton radiography is currently limited to objects with low radio-sensitivity, but possibilities for further dose reduction are presented and discussed.

Keywords: Proton imaging, Laser-ion acceleration, Monte Carlo

1 Introduction

Laser-acceleration in a plasma produces proton bunches that greatly differ from radio-frequency accelerated beams. The volume irradiated by the highly intense laser pulse represents the ion source and has dimensions of micrometres only, while the emerging bunch has large angular and energy spread. Meanwhile, kinetic energies of several tens of MeV can be achieved with 100-TW to PW laser pulses [1,2]. With the wider availability of such high-power laser systems operating at repetition rates in the order of Hz, laser-driven ion sources might in the near future become attractive not only for irradiation of cell lines [3,4], but also for small-animal irradiation. Such experiments are ideally accompanied by radiographic or even tomographic imaging prior to irradiation to ensure proper small animal positioning or to even extract a volumetric image of the stopping power relative to water for accurate treatment planning.

Conventional proton imaging for radiation oncology applications is generally based on single particle tracking [5].

* Corresponding author: Matthias Würl, Department of Medical Physics, Faculty of Physics, Ludwig-Maximilians-Universität München, Am Coulombwall 1, 85748 Garching, Germany
E-mail: Matthias.Wuerl@physik.uni-muenchen.de (M. Würl).

Z Med Phys **32** (2022) 109–119
https://doi.org/10.1016/j.zemedi.2020.05.005
www.elsevier.com/locate/zemedi

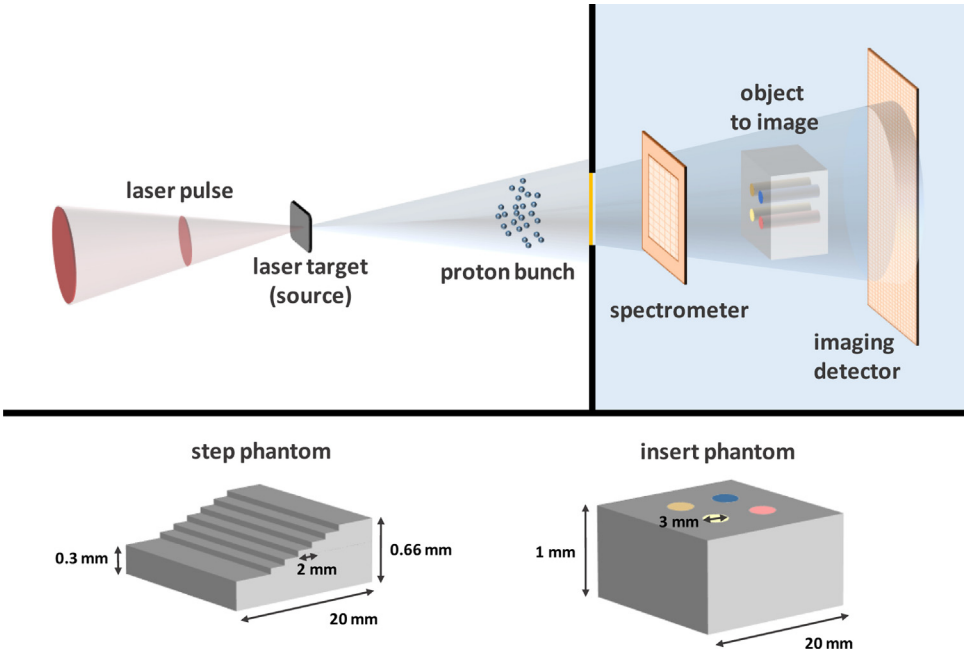

Figure 1. Schematic illustration of the proposed setup for laser-driven proton radiography and the two phantoms used for imaging. Sizes and distances are not to scale.

However, for the extremely high fluxes inherent in laser-ion acceleration, single particle tracking is far from being experimentally achievable. Due to the intrinsic energy spread though, it allows to naturally make use of a method that was originally proposed by Zygmanski et al. [6]. This approach is based on the passive energy modulation of a monoenergetic proton beam from a conventional accelerator, such that a monotonically decreasing depth-dose distribution is created. Such distribution, resembling X-ray attenuation in matter, requires a proton energy distribution where the particle number monotonically decreases with increasing kinetic energy similar to the one obtained in laser-ion acceleration in the target-normal-sheeth acceleration (TNSA) regime [7,8]. The sometimes considered disadvantageous polychromaticity of laser-accelerated proton bunches could hence prove beneficial for imaging [1].

In experimental imaging studies based on energy modulation of an initially monoenergetic beam from conventional accelerators (e.g. Zygmanski et al. [6] and Ryu et al. [9]), the water equivalent thickness (WET) of a traversed object is obtained from an a priori created calibration curve relating the detector signal to water thickness. This is not sufficient for imaging with laser-accelerated proton bunches, where the calibration curve is different for each particle bunch due to typical shot-to-shot fluctuations in the kinetic energy distribution [10]. Accurate spectrometry of each individual particle bunch is hence required to reduce uncertainties in quantitative imaging and a particular calibration curve needs to be created based on the measured energy spectrum of the specific bunch. To account for the angular divergence of the particle bunch, the used spectrometer should ideally be position-sensitive and operated in transmission prior the object to be imaged, without significantly perturbating the actual proton field.

Different from a previous work relying on offline measurement [11], we propose a setup for quantitative and online proton transmission imaging using a laser-driven proton source with proton energies up to 100 MeV. A position-sensitive spectrometer based on the time-of-flight (TOF) technique is included for an online determination of the energy distribution of the individual bunches before impinging on the object to be imaged. For imaging, a pixelated silicon detector is used. As this imaging setup should be compatible with typical laser-driven proton sources, no additional active or passive beam shaping devices are foreseen in this study. The methodology to determine the WET of an imaged object from the signal of a thin pixelated detector downstream of the object is presented. Feasibility of this setup and performance in terms of WET and spatial resolution are evaluated by means of a detailed Monte Carlo (MC) simulation, giving a framework for a future experimental setup.

2 Materials and methods

2.1 Setup overview

The proposed setup for radiography using a laser-driven proton source is illustrated in Figure 1. The laser-accelerated proton bunch propagates in vacuum before exiting the vacuum chamber through a 50 μm thin Kapton window. The first silicon detector is operated in time-of-flight configuration [12]

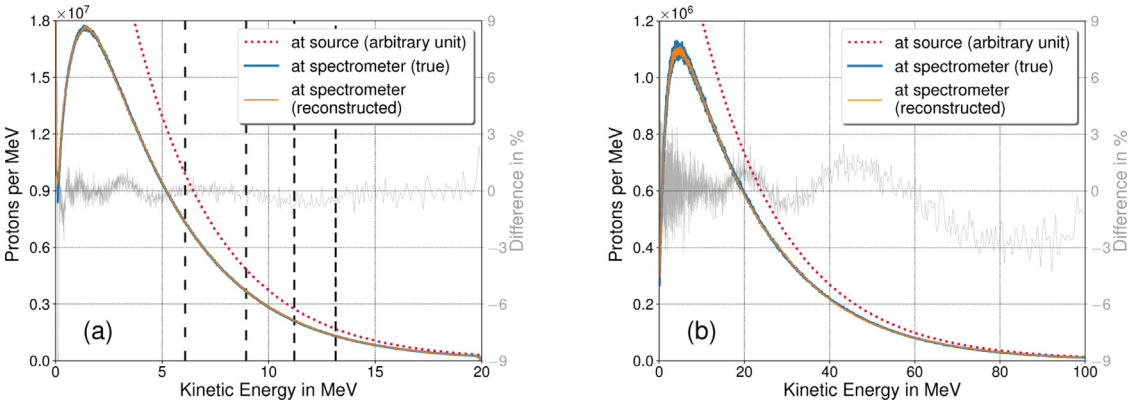

Figure 2. Proton energy distribution at the source (dotted red) and at the spectrometer (thick blue), compared to the reconstructed energy distribution (orange) for the energy interval up to (a) 20 MeV and (b) 100 MeV. The relative difference between both distributions is shown in grey (right axis). In (a), cut-off energies for WETs of 0.5, 1.0, 1.5, 2.0 mm are indicated by dashed vertical lines, respectively.

upstream of the object to determine the kinetic energy distribution of the proton bunches as an online and shot-to-shot spectrometer. With a sufficiently low thickness, an application in transmission is possible without significantly perturbing the initial proton bunch. After passing the first detector, the bunch reaches the object to be imaged. From the initial polyenergetic distribution, only protons with an energy sufficient to entirely penetrate the object are detected by a second silicon detector downstream of the object. This pixelated detector gives a spatially resolved signal, proportional to the energy deposited by the residual proton bunch. Based on this detector signal, the total energy loss along straight lines connecting the source and the detector can then approximately be calculated and converted into a quantity of interest, the WET.

The described setup was implemented in the MC code FLUKA [13,14]. In a first study, the Kapton window was removed and the entire setup was placed in vacuum.

2.2 Simulation settings

2.2.1 Proton source

Two energy intervals were examined in this study, ranging up to 20 MeV and up to 100 MeV, which corresponds to proton ranges in water of a few millimetres and some centimetres, respectively. To mimic the energy distribution of a laser-driven source, kinetic energies of the protons are sampled from an exponential distribution with a high-energy cut-off E_{cutoff}. The probability density function is

$$N(E_{\mathrm{kin}}) = \begin{cases} \lambda \exp(-\lambda E_{\mathrm{kin}}) & 0 < E_{\mathrm{kin}} \leq E_{\mathrm{cutoff}} \\ 0 & \text{else} \end{cases} \quad (1)$$

with $\lambda = 0.25\,\mathrm{MeV}^{-1}$ and $E_{\mathrm{cutoff}} = 20$ MeV for the low-energy simulations and $\lambda = 0.05\,\mathrm{MeV}^{-1}$ and $E_{\mathrm{cutoff}} = 100$ MeV for higher energies. The respective energy distributions are shown in Figure 2.

The source size in laser-ion acceleration from thin foils is typically in the order of a few μm [15,16] and was here approximated by a point source. The divergence of the proton bunches was sampled from a Gaussian distribution with a full angle of $\theta = 5^\circ$ (FWHM), which is a rather modest divergence angle for such proton sources [17,18]. Since a spatially homogeneous proton fluence would be beneficial for imaging, the choice of this small divergence angle could approach a worst case scenario. In this study, the energy distribution of the protons was assumed to be independent of the angle with respect to the central beam axis.

2.2.2 Phantoms

Two phantoms were modelled for the simulation geometry (see Figure 1) and used to assess the imaging performance. The *step phantom* consists of a $20 \times 20\,\mathrm{mm}^2$ large and 300 μm thin PMMA slab with 6 steps. Each step, except for the 5 mm wide first and last step, is 2 mm wide and 60 μm high. For the high energy interval, the slab thickness was 20 mm and the number of steps was reduced to 3, each 5 mm wide and 1 mm high.

The *insert phantom* is a $20 \times 20\,\mathrm{mm}^2$ large PMMA slab. Its thickness is 1 mm and 20 mm for the low and high energy simulations, respectively. It has four cylindrical inserts, each with a diameter of 3 mm and spanning over the entire phantom along the proton beam direction. The insert materials are skeletal muscle, compact bone, adipose tissue and water.

2.2.3 Detectors

The TOF spectrometer is modelled by a $2 \times 2\,\mathrm{cm}^2$ large and 20μm thin silicon cuboid, of which only the central area of $1.6 \times 1.6\,\mathrm{cm}^2$ and a thickness of 10 μm are considered as sensitive volume (SV) of the detector. We reasonably chose the dimensions of this hypothetical detector based on existing detector prototypes used in previous experiments [19]. The spectrometer was placed 1 m downstream of the proton source

for the low energy and 3 m for the high energy simulations. For each proton entering the SV, arrival time and lateral position, as well as energy deposition inside the SV was scored in list-mode. After runtime, the list-mode data were binned according to position and arrival time at the detector. The spatial bin width was set to $2 \times 2\,\mathrm{mm}^2$, corresponding to the pixel size of the spectrometer. This relatively coarse pixel size was chosen, because a finer pixelation implies an increased number of read-out channels and hence complexity of the system in an experimental environment. The temporal bin width was $\Delta t = 0.05$ ns, corresponding to a realistic sampling time of the read-out electronics in an experimental setup. The TOF signal in each pixel is finally mimicked by summing the energy deposition of all protons reaching that pixel within each corresponding time bin. Note that in an experimental setup, the measured TOF signal is a convolution of the here described TOF signal with the response function of the detection system [12], thus requiring deconvolution prior to spectrum reconstruction. For simplicity, no convolution and deconvolution were applied in this simulation study, i.e., the response of the detector was assumed to be instantaneous. The influence of pixel size and sampling time of the spectrometer on the quality of the reconstructed WET images and hence the requirements for a future setup is addressed of the results section.

As imaging detector, a simplified model of the CMOS-based pixel detector system RadEye, which has already been extensively used in our group for the detection of laser-accelerated particles [20,21], was included in the simulation. Energy deposition was scored in the 2 µm thin sensitive silicon layer of the detector according to a Cartesian grid with bin sizes corresponding to the pixel size of the sensor (1024×512 square pixels with a size of $48 \times 48 \times 2\,\mu\mathrm{m}^3$). A 2 µm thin SiO_2 passivation layer on top of the silicon layer was also included in the simulation geometry [22].

2.3 Reconstruction methods

2.3.1 Reconstruction of the proton spectrum

The output of each pixel of the simulated spectrometer is an array containing the signal, i.e., the total energy deposition inside that pixel, and the corresponding time array. With the signal array $\vec{S}(t)$ having n entries, the time array can be expressed either by the central time of each bin, $\vec{t}_{\mathrm{mid}}$ of size n, or by the $n+1$ bin edges, $\vec{t}_{\mathrm{edge}}$. Both time arrays were then converted into the corresponding kinetic proton energies according to

$$\vec{\mathcal{E}}_{\mathrm{mid}}(\vec{t}_{\mathrm{mid}}) = \left(\frac{1}{\sqrt{1 - \left(\frac{z}{c\vec{t}_{\mathrm{mid}}}\right)^2}} - 1 \right) \cdot m_{\mathrm{p}} c^2 \qquad (2)$$

and analogous for $\vec{\mathcal{E}}_{\mathrm{edge}}$. The TOF distance, i.e. the distance between proton source and spectrometer is denoted by z, whereas c and m_{p} are the speed of light and the proton rest mass, respectively.

In order to obtain the number of protons within each energy bin i, $N_{\mathrm{p},i}$, the simulated spectrometer signal S_i was divided by the corresponding average energy deposition of protons within the $d = 10$ µm thin silicon SV, $\langle E_{\mathrm{dep},i}(d) \rangle$. This average energy deposition was calculated as a function of kinetic proton energy by means of MC simulations.

In a final step, the resulting spectrum was corrected for the actual energy loss inside the total thickness of the spectrometer ($d = 20$ µm silicon). This was done by shifting all energy bin edges $\mathcal{E}_{\mathrm{edge},i}$ (and the central energies of each bin, $\vec{\mathcal{E}}_{\mathrm{mid}}$) towards lower energies. The energy dependent shift, calculated by

$$\mathcal{E}_{\mathrm{shift},i}(\mathcal{E}_{\mathrm{edge},i}) = \langle E_{\mathrm{dep}}(\mathcal{E}_{\mathrm{edge},i}; d) \rangle$$

was also estimated relying on MC simulations. Bins with final edge energies $\mathcal{E}_{\mathrm{edge},i} \leq 0$ were deleted.

Although the described procedure relies on the assumption that the actual energy deposition of one proton is close to the average energy deposition $\langle E_{\mathrm{dep}}(\mathcal{E}_{\mathrm{mid},i}; d) \rangle$, the performance of the reconstruction has shown to be sufficient (Figure 2). Differences between the reconstructed proton energy distribution and the actual spectrum recorded behind the spectrometer are typically below 1% and 2% for the low and the high energy interval, respectively. Only for the very low and high energy bins in both intervals, deviations tend to be larger. However, in the energy range where the highest contribution to the signal in the imaging detector is expected (5 MeV to 15 MeV for the low-energy study), the agreement between reconstructed and true spectrum is adequate. The encountered fluctuations are due to statistical fluctuations in the energy deposition inside the detector SV and their impact on the WET reconstruction (see next section) is expected to be negligible.

2.3.2 Reconstruction of the WET

Due to the decaying shape of the proton energy distribution, the detectable signal in the imaging detector is monotonically decreasing with increasing WET of the traversed object. Thus, a smaller WET of the traversed object results in a larger energy deposition in the sensitive volume of the imaging detector.

The particle bunch specific conversion curve relating the signal in the imaging detector to the WET of the object is relying on a look-up table that assigns the traversed WET to the *expected* energy loss of *one* proton of a specific energy inside the SV of the imaging detector pixel. This average energy loss, $\langle E_{\mathrm{dep}}(\mathrm{SV}, E_{\mathrm{kin}}, \mathrm{WET}) \rangle$, was calculated only once, using a large set of FLUKA MC simulations scoring the energy deposition inside the imaging detector after a block of water. The thickness of the water block, as well as the initial kinetic energy was varied within this set of simulations and a cubic spline fit to the resulting data was performed to generate a finer

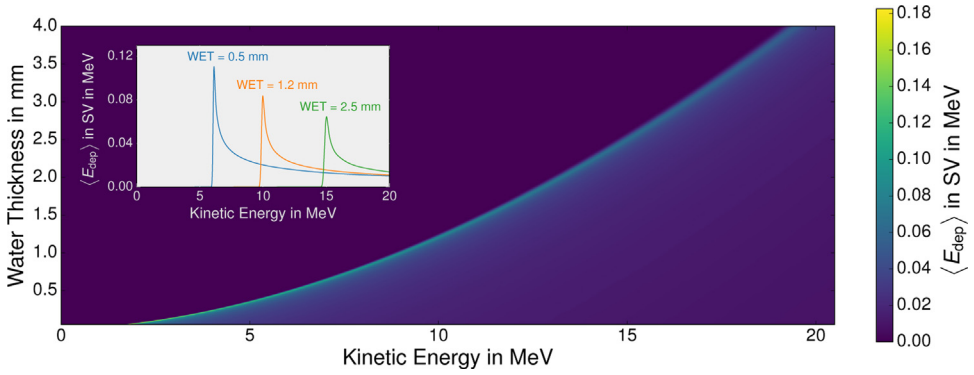

Figure 3. Graphical representation of the look-up table for the WET determination, relating the expected energy loss $\langle E_{\mathrm{dep}}(\mathrm{SV}\,;E_{\mathrm{kin}}\,;\mathrm{WET})\rangle$ inside SVs of the RadEye detector pixels to the proton energy E_{kin} and the WET. Profiles for three different water thicknesses are shown exemplary in the inset.

resolution of the look-up table. Figure 3 shows a graphical representation of the look-up table for the lower energy range.

For a proton fluence that is not laterally homogeneous along the entire detector surface, the conversion curve relating detector signal to WET is not only changing with each proton bunch but may also differ for different pixels of the imaging detector. Therefore, such conversion curve was created analytically prior to the WET reconstruction for each detector pixel. First, the number of protons and the energy spectrum that would be expected to reach each detector pixel in an open field configuration, was calculated. This computation is based on the previously already reconstructed spectrum, the geometrical size of the pixels and the divergent beam, taking into account the distances from source to spectrometer and from source to imaging detector. Then, the look-up table was used to create one conversion curve for each pixel of the imaging detector. The WET of the respective pixel is then considered to be that point of the conversion curve which is closest to the detector signal. The look-up table data was generated from the energy-deposition inside the imaging detector after having traversed a block of water, with scattering and fluence reduction due to nuclear effects inherently taken into account.

With a sensitive thickness of only 2 µm, statistical fluctuations in the energy deposition within each $48 \times 48\ \mu\mathrm{m}^2$ small pixel of the RadEye detector may be large, especially if the total number of protons per image detector pixel is small. For this reason, as well as for computational reasons, 2×2 adjacent pixels were combined to one *macro-pixel* with a pixel size of $96 \times 96\ \mu\mathrm{m}^2$. Moreover, a median filter was applied to the energy deposition in the detector prior to WET reconstruction in order to further minimize the effect of statistical fluctuations.

2.4 Assessment of the image quality

2.4.1 Density/WET resolution

Two quantities were used to assess the density resolution of the obtained WET distributions. First, the *mean WET* of defined regions-of-interest (ROIs) was calculated. Each ROI includes only one certain material or one step thickness. Since the interfaces between two materials or two steps are largely affected by multiple Coulomb scattering (MCS), a margin between the interfaces and the ROIs was introduced. Pixels closer than 0.3 mm and 0.5 mm to these interfaces for the lower and higher energy intervals, respectively, were hence excluded from the ROIs.

On a pixel scale, the accuracy was quantified by calculating the root-mean-square error,

$$\mathrm{RMSE} = \sqrt{\frac{\sum_i^n (\mathrm{WET}^i_{\mathrm{recon}} - \mathrm{WET}^i_{\mathrm{true}})^2}{n}} \tag{3}$$

which was done for the entire object (*global RMSE*), as well as taking into account only pixels from given ROIs. The normalized RMSE, *NRMSE*, was obtained for the ROIs by dividing the RMSE by the true WET.

2.4.2 Spatial resolution

For assessing the spatial resolution of the reconstructed WET images, a sigmoidal curve, described by

$$f(x) = a_1 + \frac{a_2}{1 + \exp\left(-\frac{x - a_3}{a_4}\right)} \tag{4}$$

was fitted to the WET values arranged on a line perpendicular to the interface between two adjacent steps of the step phantom [23]. The fit parameter a_1 is the starting value of the sigmoidal curve, hence the WET of the thinner step. The sum $a_1 + a_2$ is the ending value, i.e. the WET of the thicker step. The remaining fit parameters a_3 and a_4 correspond to the position and the width of the inflection. To minimize the impact of fluctuations, the mean of the WET image along the axis parallel to the step interfaces was calculated prior to the fitting procedure. The spatial distance between the 25%- and the 75%-value of the sigmoidal fit was then taken as the

FWHM of a Gaussian line-spread function (LSF). A Gaussian was chosen, since this function properly describes the LSF in proton radiography [23]. The optical transfer function (OTF) was then calculated by normalizing the discrete Fourier transform of the LSF, and the modulation transfer function (MTF) was finally obtained by taking the magnitude of the OTF. The 10% value of the MTF, $MTF_{10\%}$, is expressed in line-pairs per mm ($lp\,mm^{-1}$) and was used to characterize the spatial resolution. This calculation was done for all interfaces between adjacent steps and the spatial resolution values given hereafter refer to the mean and its standard deviation.

3 Results

3.1 Proton radiographies at low energies

With a divergence angle of $\theta = 5°$, only about 4.5% of the primary protons created in the source reach the $2 \times 2\,cm^2$ large area of the 1 m distant spectrometer. Due to scattering and stopping of low-energy protons inside the spectrometer, the fluence decreases further such that only 3.3% of the protons impinge on the phantom. As the imaging technique relies on the stopping of low-energy protons inside the phantom, the number of protons actually reaching the imaging detector is further reduced, depending on the object material and thickness. For a primary proton number of 10^9, only a few tens up to around one hundred protons contribute to the signal in a macro-pixel of the detector 5 mm downstream of the insert phantom. This corresponds to a fluence in the detector plane of 4.8×10^5 - 1.2×10^6 protons/cm^2.

WET distributions with profiles of step and insert phantom are shown in Figure 4a and b. Within all five ROIs of the insert phantom, the average reconstructed WET differs by less than 1.5% from the true WET and the NRMSE is below 3%. The RMSE for a field-of-view (FOV) equal to the size of the spectrometer, divided by the geometrical thickness of the phantom, was found to be 3.5%.

Spatial resolution is mainly limited by MCS inside the phantom, introducing a blurring of the image. Evidently, this blurring increases with the thickness of the imaged object and the gap between it and the detection system. The spatial resolution was therefore examined as a function of distance between object and detector with a fixed number of primary particles of 10^9. In Figure 4c and d, WET distributions for distances of 1 mm and 20 mm are shown together with the laterally averaged WET values at the interface of the fourth and fifth steps. All edges of the step phantom are very well preserved at the smallest gap while at a distance of 20 mm the image is notably more blurred. Yet, the 2 mm wide steps can still be visually distinguished. Spatial resolution as a function of distance is shown in Figure 4e. For a 5 mm gap between phantom and detector, which seems a reasonable distance for experimental imaging of such small samples, the spatial resolution is $(2.5 \pm 0.2)\,lp\,mm^{-1}$. In case of a ten times higher proton fluence where combining 2×2 pixels prior to the WET determination would not be required due to better statistics, an even better spatial resolution of $(3.1 \pm 0.3)\,lp\,mm^{-1}$ could be achieved for the same distance.

The high absorption and energy losses inside the phantom give rise to the previously reported excellent WET resolution. However, this comes at the price of rather high radiation dose in the object to be imaged. The dose deposition in the insert phantom for 10^9 primary protons was 43 mGy. A further decrease in the primary particle number results in rapidly increasing RMSE values and differences between the average reconstructed WETs and true WETs, as shown in Figure 5a.

As a consequence of the exponentially decaying shape of the proton energy distribution and the resulting depth-dose distribution, the total imaging dose decreases with larger phantom thickness, while the dose close to the front surface of the object remains constant. Conversely, that implies that introducing additional material upstream of the phantom results in a hardening of the incoming energy distribution and can thus reduce the dose deposited in the object. When moving the imaging setup from vacuum to air, this is naturally achieved by inserting a thin vacuum window and air. For the same imaging conditions as previously described, this reduces the imaging dose by more than 20%. Depth-dose curves for the insert phantom are shown for the vacuum and the air-filled setup in Figure 5b.

The additional tabulated energy losses inside the Kapton foil and the short air gap between foil and spectrometer introduce a further source of uncertainty to the spectrum reconstruction. However, increased differences in the spectrum are most pronounced at proton energies below 5 MeV, which for the phantom thickness used in this study do not contribute to the signal in the imaging detector.

When taking into account the additional 1 cm air between spectrometer and imaging detector, the difference between the mean reconstructed WET and the true WET is still well below 1.5% for the five respective materials. Also RMSE values for the ROIs (<3%), as well as for the entire object (3.4%), are hardly affected by the additional Kapton foil and air. Moreover, no significant difference in the spatial resolution was found between the setup in vacuum and in air.

3.2 Requirements on the spectrometer resolution

Inaccuracies in the reconstructed proton energy distribution are among the major sources of uncertainty for the WET determination. The temporal resolution of the TOF spectrometer directly affects the energy resolution of the resulting spectrum. Furthermore, if the proton field at the phantom location is not homogeneous along the transversal dimensions, the spatial variation of the spectrum has to be measured as well, i.e., pixelation of the TOF spectrometer may be necessary.

For divergence angles >8°, the spatial proton distribution within a $2 \times 2\,cm^2$ large plane at the phantom location 1 m downstream of the source can be considered rather uniform with deviations from the mean fluence below 1%. For lower

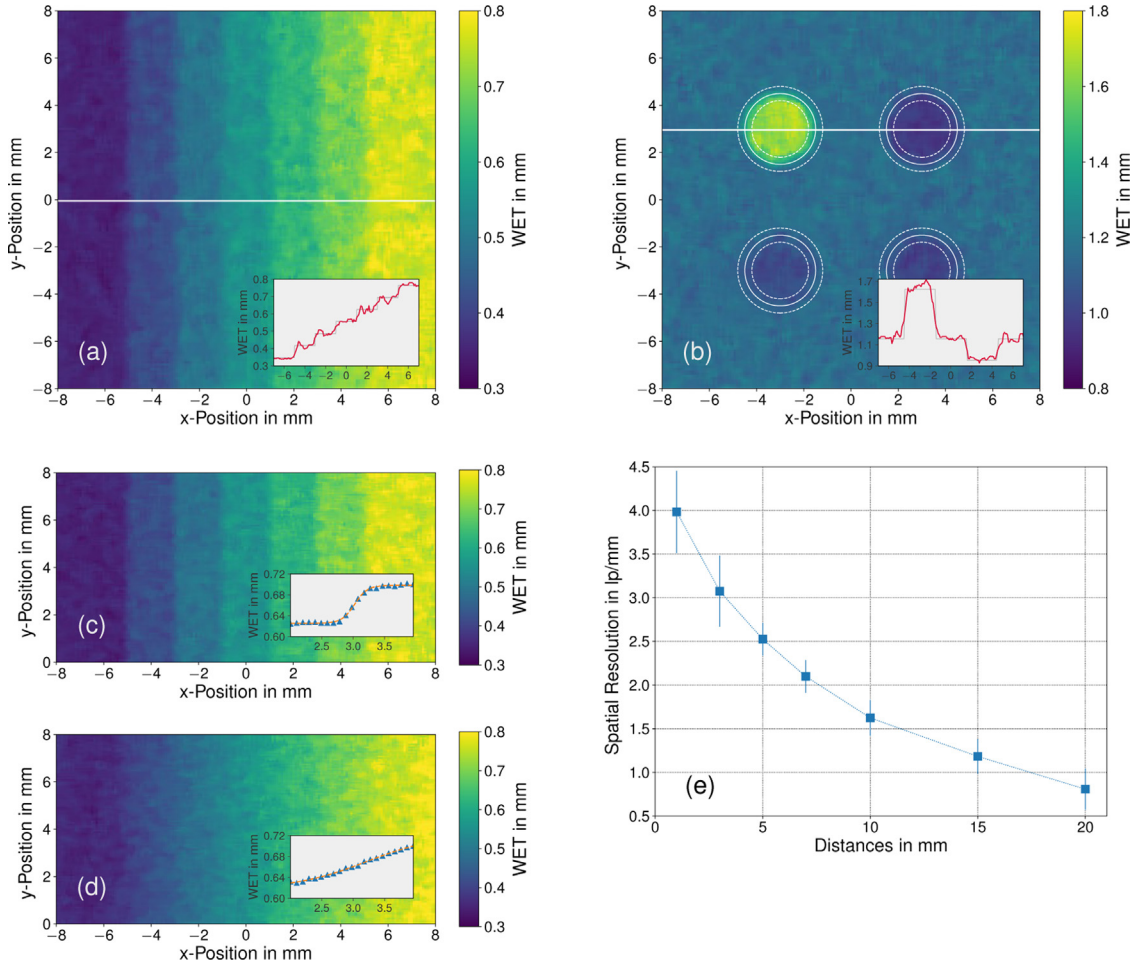

Figure 4. Reconstructed WET distribution of the (a) step and the (b) insert phantom for energies up to 20 MeV. The white horizontal lines mark the locations of the 1D profile, shown red in the inserts where they are compared to the true WET (grey). The dashed white circles in (b) indicate the borders of the ROIs, the solid circle marks the actual material interfaces. In (c) and (d), WET distribution of the step phantom for a distance of 1 mm and 20 mm between phantom and detector are shown. The respective mean WET values along the x-axis (triangles) with fits according to Eq. (4) (orange dashed line) are shown in the insets. (e) Spatial resolution as a function of distance between phantom and detector.

beam divergence, smaller source-to-phantom distances and/or a larger FOV, fluence variations along the FOV of several percent may become important. Since these variations directly affect the WET calculation, especially at the center and the edges of the FOV, this would result in wrong WET values unless the spectrum is determined spatially resolved. Therefore, the influence of spectrometer pixel size and sampling time on the resulting WET resolution was studied for the low-energy case, in order to determine hardware requirements of the TOF spectrometer for potential imaging applications.

The effect caused by a non-homogeneous proton field on the reconstructed WET distribution was determined for a proton beam with a divergence angle of 5°, by gradually increasing the pixel size of the spectrometer from 1 mm to 16 mm. Practically no difference between a pixel size of $8 \times 8\,\mathrm{mm}^2$ and no pixelation ($\hat{=}$ $16 \times 16\,\mathrm{mm}^2$ pixel size) was found due to the point symmetry of the simulated proton beam and the symmetric spectrometer pixel arrangement.

For spectrometer pixel sizes $\leq 4 \times 4\,\mathrm{mm}^2$, only minor differences in the calculated WET values were found. For large pixel sizes ($\geq 8 \times 8\,\mathrm{mm}^2$), an underestimation in the center of -0.6% and an overestimation at the edges of the FOV of $+1.8\%$ was found. The relative differences between the mean reconstructed WET of the thinnest, the central and the thickest steps and the corresponding true WET for different spectrometer pixel sizes are summarized in Figure 6.

Increasing the temporal bin width, i.e., decreasing the resolution of the retrieved energy distribution results in a systematic overestimation of the WET. However, an increase by a factor of 4, corresponding to a sampling time of 0.2 ns, shows only a moderate overestimation (+1.6%) for TOF distance, low energy range and millimetre phantom thickness as used

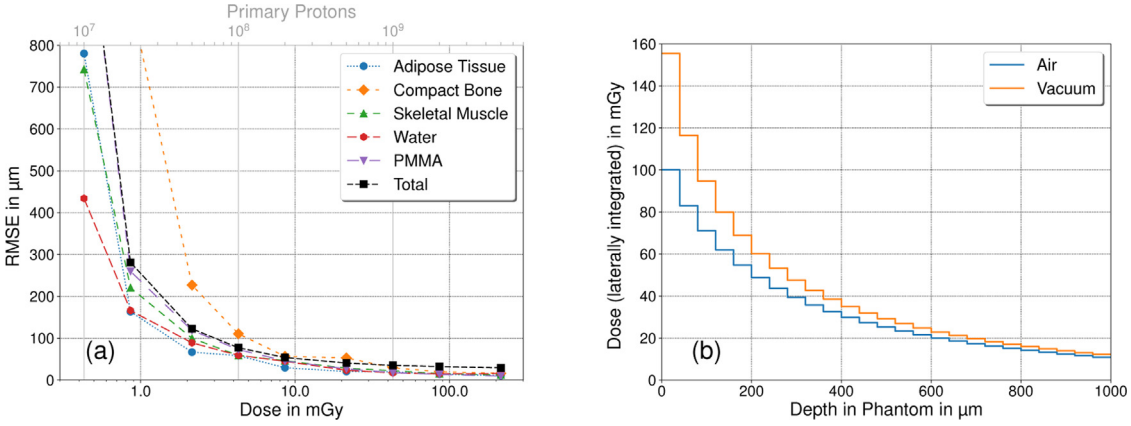

Figure 5. (a) Image quality as a function of imaging dose for the insert phantom in vacuum and low proton energies. The RMSE of the reconstructed WET of the total object (black) and the materials (colors) are plotted versus the number of primary particles (upper axis) and the corresponding dose (lower axis). Dashed lines are to guide the eye. (b) Depth-dose distribution inside the insert phantom for the low-energy proton radiography entirely in vacuum (orange) compared to the radiography setup in air (blue) for 10^9 primary protons.

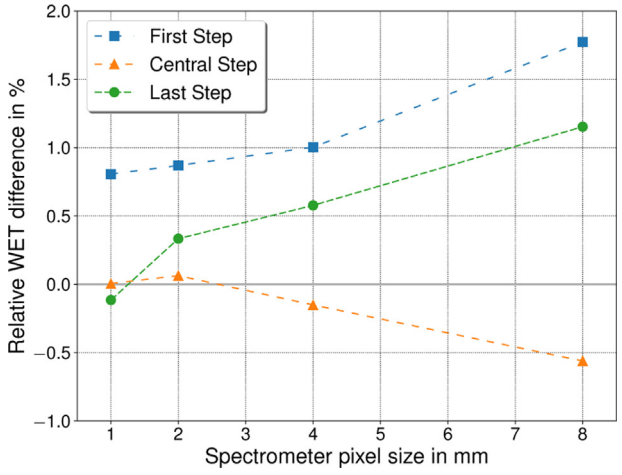

Figure 6. Relative difference between mean reconstructed and true WET for three different steps as a function of spectrometer pixel size.

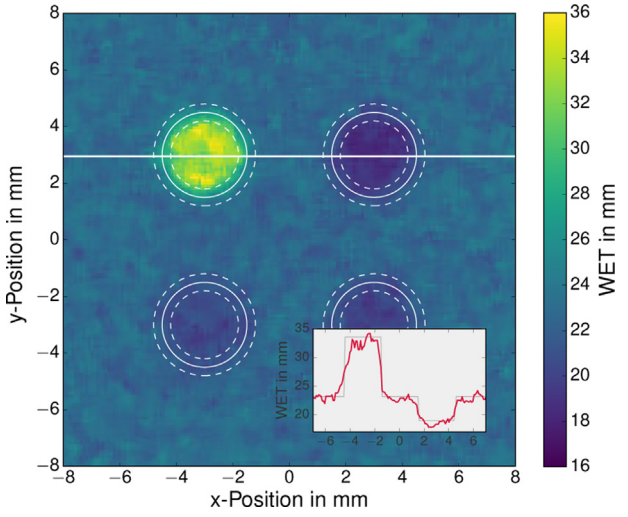

Figure 7. WET distribution of the 2 cm thick insert phantom for 10^{10} primary protons. The white horizontal line indicates the position of the profile plotted red in the inset, where it is compared to the true WET (grey).

in this study. Increasing the sampling time further to 0.5 ns then leads to a WET overestimation of up to almost 3%. In contrast, a reduction of the sampling time from the initial value of 0.05 ns down to 0.01 ns did not reveal any benefit in the reconstructed image.

3.3 Radiography at higher proton energies

Increasing the proton energy up to 100 MeV allows imaging of objects with thickness in the order of centimetres, making it hence suitable for small-animal radiography. Simulations of the imaging setup in air were performed with 10^9 exponentially distributed primary protons, resulting in a mean proton number reaching the detector macro-pixels between 40 and 110. The corresponding imaging dose for one radiography was 13.7 mGy.

The reconstructed WET distribution with a profile plot through two of the inserts is shown in Figure 7. Although the different inserts can clearly be distinguished, an increased blurring of the image is evident, caused by the larger impact of scattering within the phantom as compared to the thinner phantoms previously investigated. The spatial resolution at high energies, determined using a 2.0 to 2.3 cm thick step phantom, was found to be $(1.9 \pm 0.6)\,\mathrm{lp\,mm^{-1}}$ for a distance between phantom and RadEye of 5 mm.

The global RMSE was 0.86 mm, corresponding to 4.2% of the geometrical phantom thickness, while the NRMSE values within the ROIs were found to be small (1.8–2.3%). Although still sufficiently low, the largest NRMSE was found for the bone insert. This can easily be explained by the increased

scattering, lowering the reconstructed WET of the bone insert close to the interface with water. Agreement between the mean WET in the ROIs and the true WET for higher proton energies was found to be better than 1.1%.

4 Discussion

4.1 Performance and possible limitations of our proposed setup

For a primary proton number of 10^9 in the studied configuration, the mean reconstructed WET within each ROI was found in very promising agreement with ground truth WET values. The reported relatively low RMSE values within each ROI indicate a quite high precision, despite the relatively small pixel size of roughly 0.1 mm and the therefore low number of particles contributing to the signal in the detector pixels. Images of such density resolution require a rather high dose deposition of some tens of mGy inside the object to be imaged. Especially the entrance dose at the front surface of the phantom is prohibitively large (see Figure 5b), as in biomedical applications low imaging doses are generally desired. In the current setup, a further expansion from radiographic to tomographic imaging, where several projections are needed, might therefore only be an option for objects that are insensitive to radiation dose.

Nevertheless, dose reduction down to biologically acceptable values while still maintaining a decent image quality might be possible. The high dose is a result of the exponential-like energy spectrum of the laser-driven ion source. For example, in order to entirely penetrate a 0.5 mm thick water phantom, proton energies $\gtrsim$6 MeV are required. However, more than two third of the protons from the input spectrum as implemented in our study have a kinetic energy below 6 MeV and will therefore not contribute to the measured signal. Removing all protons with kinetic energies lower than 5 MeV before reaching the spectrometer would hence lead to a dose reduction by almost 50%, while the image quality would not be affected at all. This beam hardening could be achieved either actively by a magnetic chicane or passively by additional absorbing material prior to the phantom, which in turn might have an impact on the image quality due to scattering inside the absorber. When moving the imaging setup from vacuum to air, the vacuum window and the additional air gap act as additional absorber and imaging dose could be reduced considerably. In our study, hardly any relevant degradation of the image quality was encountered. Additional scattering in the air gap between the phantom and imaging detector can therefore be neglected for a distance between phantom and detector of 5 mm, but could further increase with larger distances. On the other hand, imaging dose could considerably be reduced.

In applications where reduced image quality is acceptable, proton fluence and hence the dose can easily be reduced by a factor of 10. The resulting NRMSE is still within 10%, thus moderate density or thickness differences in the object can still be detected and it can therefore serve as reliable tool for e.g. sample alignment. The most reliable method to reduce the fluence in an experiment at a laser-driven ion source would be to shift the imaging device further away from the source. Comparable doses as reported for proton imaging based on time-resolved dose measurement in Jee et al. [24] could hence be realistic for a similar quality of the radiographs, taken with one single laser-accelerated proton bunch.

The spatial resolution of proton radiography is mainly limited by MCS inside the object, as also discussed in Zygmanski et al. [6]. Distances between phantom and imaging detector should therefore be as small as reasonably achievable. A good compromise between spatial resolution and experimental applicability for the here presented imaging of thin phantoms with macroscopic inhomogeneities might be a distance of 5 mm.

For phantom thicknesses of some centimetres, corresponding to potential small-animal irradiations, proton energies up to 100 MeV are required. Increased scattering inside the phantom itself results in substantially larger image blurring, which is most pronounced at the interfaces between high- and low-WET material. Although the spatial resolution decreases for the thicker phantom, sub-mm resolution was still obtained with an air gap between phantom and detector of 5 mm. With the introduction of larger margins defining the ROIs to take into account the increased scattering (at the cost of smaller ROIs), the correct WET could still be assigned to the respective insert materials. Potentially, the image quality in terms of spatial resolution might be improved by complementing the WET determination process with a deconvolution step. Based on the primarily reconstructed WET distribution and the initial proton spectrum, energy- and WET-dependent scatter components of the detector signal can be estimated and deconvolved from the measured signal. However, further investigations on the potential of this method are beyond the scope of this study.

Due to the method used to create the look-up tables for WET determination, large-angle scattering and fluence reduction due to nuclear reactions are inherently taken into account in the reconstruction, considering material with properties similar to water. However, it has to be stressed that the look-up table is based on the assumption that the proton fluence is laterally homogeneous over an area that is large compared to the pixel size. This will certainly not be true close to the interfaces between materials with very large WET differences, e.g. between the phantom and air.

In laser-ion acceleration, X-rays, gammas, fast electrons and heavier ions are typically co-emitted with the proton bunch. No detailed investigations were performed within this study to assess their impact on the final image quality. For the same energy per nucleon, the energy loss rate is considerably larger for ions heavier than protons. The number of heavy ions having a sufficiently high energy to traverse the object to be imaged can therefore assumed to be small. However, their contribution to the imaging dose needs to be taken into

account. Nevertheless, provided that different ions can be distinguished within the spectrometer, their additional signal in the imaging detector could be accounted for by including their energy deposition versus water thickness to the conversion curves. In contrast, for X-rays and gammas, this correction method would not be possible. However, the RadEye sensor is rather insensitive to photons in that energy range due to its low sensitive thickness. According to MC simulations, the range in water of 10 MeV electrons is around 5 cm. Hence, although detection efficieny for electrons in the detector is also low [21], the signal contribution by electrons could become more perturbing for quantitative imaging. An almost complete removal of electrons from the mixed particle beam could be achieved by including a dipole magnet with a very shallow magnetic field (e.g. 50 mT) perpendicular to the beam direction, upstream of the imaging setup. Such magnetic field over a dipole length of 10 cm, followed by a drift space of 10 cm prior to the spectrometer would lead to a lateral displacement of 10 MeV electrons of 21.6 mm, while the displacement of protons in the other direction would be 2.3 mm and 1.2 mm for 5 MeV and 20 MeV, respectively. Given the broad proton field, a continuously decaying conversion curve for the WET reconstruction is still maintained since the displacement differences for protons in the energy range of interest is small. Of course, the previously stated assumption of a laterally homogeneous proton energy distribution would then be corrupted and a pixelated spectrometer would be required. Nevertheless, the necessity of such dipole magnets needs to be studied based on measured absolute proton and electron distributions in the laser-accelerated particle bunches. If required, a more detailed simulation study based on these numbers could provide important information for a proper choice of the magnetic field strengths, positions and distances.

4.2 Considerations on the spectrometer

The divergence of the proton beam gives rise to a non-uniform proton field at the phantom. At a distance of 1 m and a full beam divergence angle $\theta = 5°$, this results in a fluence variation of up to 2.5% within a $2 \times 2\,cm^2$ plane. Although the assumption of a homogeneous fluence within this area gives rise to an only modest additional error in the reconstructed WET values (<3%), more accurate results are obtained if the spectrometer itself is pixelated. The required pixel size strongly depends on the beam divergence angle and the geometry of the setup, namely the desired FOV and the source-to-phantom distance. For divergence angles down to $\theta \approx 5°$, a distance of source to imaging setup of 1 m and a FOV of $16 \times 16\,mm^2$, a pixel size of $4 \times 4\,mm^2$ has shown to be sufficient to keep the impact of the non-uniform proton field low. With a FOV as in our study, this would hence result in 16 channels for which the TOF signal has to be acquired and converted to an energy spectrum independently. As a way to reduce the number of channels to be read out and evaluated, the use of a strip detector as transmission TOF spectrometer could prove beneficial, if the fluence distribution is cylindrically symmetric.

For the propagation distances used in our study at energies up to 20 MeV, a temporal resolution of the TOF spectrometer of 0.2 ns appears to be sufficient. Neglecting effects of spatial inhomogeneities in the proton field, this result would also be applicable to a reduction of the drift space from 1 m down to 0.25 m when keeping the temporal resolution at 0.05 ns. Equivalently, increasing the drift space to 4 m loosens the requirements in the data acquisition system in a way that a sampling time of 0.2 ns would be sufficient for a precision and accuracy better than 3% in this energy interval. It has to be stressed, though, that in this MC study the detector response was assumed to be instantaneous and the finite detector response function was hence not taken into account. Nevertheless, if the detector is well characterized and its response is known, the response can be included in the spectral reconstruction in a straight-forward manner as described in Würl et al. [12]. It remains to be shown, however, to which extent the additional uncertainty of this spectrum reconstruction has an impact on the reconstructed image quality.

Furthermore, the lateral energy distribution is assumed to be constant in this study. According to experimental studies, the higher energy components are situated closer to the central beam axis [7]. The previously drawn conclusions on the spectrometer pixel size may therefore not be entirely reliable in a real experimental setup and demands further investigation. Also, if additional active beamline elements are included in an experimental setup, the lateral energy and fluence distribution at the imaging setup might have larger variations. It is therefore crucial to either have a reliable model of the proton bunch at the location of the phantom, or to determine the spectrum with a fine spectrometer pixel size.

5 Conclusion

A detailed MC simulation study was performed to assess the feasibility of laser-driven proton radiography using a CMOS-based pixel detector and a silicon TOF spectrometer in transmission prior to the phantom. For an imaging dose of some tens of mGy, reconstructed WET values are in good agreement with ground truth WET values and at experimentally reasonable distances between object and imaging detector of around 5 mm, sub-mm spatial resolution was found for both proton energy intervals examined in this study. Moreover, no significant difference was found for both the spatial and the density resolution between the imaging setup in vacuum an in air.

The impact of the mixed radiation field on the reconstructed WET images was not investigated in detail in this study. However, the influence of heavy ions, photons and electrons is estimated to be rather small, given the thin sensitive detector layer. Nevertheless, their presence can significantly contribute to the imaging dose and hence needs to be estimated and taken into account.

The major drawback of using such a broad proton energy distribution with exponentially decaying shape is the high dose that is required to obtain the high spatial and density resolution mentioned before. This limits the presented method to applications, where the dose to the object is not of concern, especially when tomographic imaging is desired. However, a slight dose reduction while practically maintaining the same image quality can be obtained by tailoring the incoming energy distribution of the bunch, e.g. by introducing foil-like absorbers for beam hardening which are thick enough to fully stop the large number of low-energy protons, yet thin enough to only moderately reduce the proton energy of the higher energetic part of the incoming exponential energy distribution.

Conflicts of interest

The authors declare no conflicts of interest.

Acknowledgements

This work was supported by the Deutsche Forschungsgemeinschaft (DFG) Cluster of Excellence Munich-Centre for Advanced Photonics (MAP). M. Würl acknowledges financial support from the International Max Planck Research School of Advanced Photon Science (IMPRS-APS), C. Gianoli acknowledges funding from the DFG project "Hybrid imaging framework in hadrontherapy for adaptive radiation therapy' (grant # 372393016). We want to thank Prof. Anatoly Rosenfeld and Dr. Sabine Reinhardt for fruitful discussions in the early phase of this project.

References

[1] Schreiber J, Bolton PR, Parodi K. Invited review article: "Hands-on" laser-driven ion acceleration: a primer for laser-driven source development and potential applications. Rev Sci Instrum 2016;87(7):071101, http://dx.doi.org/10.1063/1.4959198.

[2] Higginson A, Gray R, King M, Dance R, Williamson S, Butler N, et al. Near-100 MeV protons via a laser-driven transparency-enhanced hybrid acceleration scheme. Nat Commun 2018;9:724.

[3] Kraft SD, Richter C, Zeil K, Baumann M, Beyreuther E, Bock S, et al. Dose-dependent biological damage of tumour cells by laser-accelerated proton beams. New J Phys 2010;12(August (8)):085003, http://dx.doi.org/10.1088/1367-2630/12/8/085003.

[4] Bin J, Allinger K, Assmann W, Dollinger Günther, Drexler GA, Friedl AA, et al. A laser-driven nanosecond proton source for radiobiological studies. Appl Phys Lett 2012;101(24):243701, http://dx.doi.org/10.1063/1.4769372.

[5] Johnson RP. Review of medical radiography and tomography with proton beams. Rep Prog Phys 2018;81(1):016701 http://stacks.iop.org/0034-4885/81/i=1/a=016701.

[6] Zygmanski P, Gall KP, Rabin MSZ, Rosenthal SJ. The measurement of proton stopping power using proton-cone-beam computed tomography. Phys Med Biol 2000;45(2):511 http://stacks.iop.org/0031-9155/45/i=2/a=317.

[7] Snavely RA, et al. Intense high-energy proton beams from petawatt-laser irradiation of solids. Phys Rev Lett 2000;85:2945–8, http://dx.doi.org/10.1103/PhysRevLett.85.2945.

[8] Wilks SC, Langdon AB, Cowan TE, Roth M, Singh M, Hatchett S, et al. Energetic proton generation in ultra-intense laser-solid interactions. Phys Plasmas 2001;8(2):542–9, http://dx.doi.org/10.1063/1.1333697.

[9] Ryu H, Song E, Lee J, Kim J. Density and spatial resolutions of proton radiography using a range modulation technique. Phys Med Biol 2008;53(19):5461 http://stacks.iop.org/0031-9155/53/i=19/a=012.

[10] Ying G, Jianhui B, Daniel H, Christian K, Jens H, Martin S, et al. An automated, 0.5 Hz nano-foil target positioning system for intense laser plasma experiments. High Power Laser Sci Eng 2017;5:E12.

[11] Roth M, Blazevic A, Geissel M, Schlegel T, Cowan TE, Allen M, et al. Energetic ions generated by laser pulses: a detailed study on target properties. Phys Rev Spec Top: Accel Beams 2002;5:061301, http://dx.doi.org/10.1103/PhysRevSTAB.5.061301.

[12] Würl M, Englbrecht F, Lehrack S, Gianoli C, Lindner F, Rösch T, et al. Time-of-flight spectrometry of ultra-short, polyenergetic proton bunches. Rev Sci Instrum 2018;89(12):123302, http://dx.doi.org/10.1063/1.5052059.

[13] Ferrari A, Sala PR, Fassó A, Ranft J. FLUKA: a multi-particle transport code. CERN-2005-10, INFN/TC_05/11, SLAC-R-773; 2005.

[14] Böhlen TT, Cerutti F, Chin M, Fasso A, Ferrari A, Ortega PG, et al. The FLUKA code: developments and challenges for high energy and medical applications. Nucl Data Sheets 2014;120:211–4.

[15] Cowan TE, Fuchs J, Ruhl H, Kemp A, Audebert P, Roth M, et al. Ultralow emittance, multi-mev proton beams from a laser virtual-cathode plasma accelerator. Phys Rev Lett 2004;92(May):204801, http://dx.doi.org/10.1103/PhysRevLett.92.204801.

[16] Schreiber J, Kaluza M, Grüner F, Schramm U, Hegelich BM, Cobble J, et al. Source-size measurements and charge distributions of ions accelerated from thin foils irradiated by high-intensity laser pulses. Appl Phys B 2004;79(December (8)):1041–5, http://dx.doi.org/10.1007/s00340-004-1665-5. ISSN 1432-0649.

[17] Nürnberg F, Schollmeier M, Brambrink E, Blažević A, Carroll DC, Flippo K, et al. Radiochromic film imaging spectroscopy of laser-accelerated proton beams. Rev Sci Instrum 2009;80(3):033301, http://dx.doi.org/10.1063/1.3086424.

[18] Bin JH, Ma WJ, Allinger K, Wang HY, Kiefer D, Reinhardt S, et al. On the small divergence of laser-driven ion beams from nanometer thick foils. Phys Plasmas 2013;20(7):073113, http://dx.doi.org/10.1063/1.4816031.

[19] Würl M, Reinhardt S, Rosenfeld A, Petasecca M, Lerch M, Tran L, et al. Experimental studies with two novel silicon detectors for the development of time-of-flight spectrometry of laser-accelerated proton beams. J Phys: Conf Ser 2017;777(1):012018.

[20] Reinhardt S, Draxinger W, Schreiber J, Assmann W. A pixel detector system for laser-accelerated ion detection. J Instrum 2013;8(03):P03008.

[21] Lindner F, Bin J, Englbrecht F, Daniel H, Paul B, Ying G, et al. A novel approach to electron data background treatment in an online wide-angle spectrometer for laser-accelerated ion and electron bunches. Rev Sci Instrum 2018;89(1):013301.

[22] Reinhardt S. Detection of laser-accelerated protons. PhD thesis. LMU München; 2012.

[23] Seco J, Oumano M, Depauw N, Dias MF, Teixeira RP, Spadea M. Characterizing the modulation transfer function (MTF) of proton/carbon radiography using Monte Carlo simulations. Med Phys 2013;40:091717.

[24] Jee K-W, Zhang R, Bentefour EH, Doolan PJ, Cascio E, Sharp G, et al. Investigation of time-resolved proton radiography using X-ray flat-panel imaging system. Phys Med Biol 2017;62(5):1905.